Optimal Design Approach for One-dimensional Rubber-Concrete Periodic Foundations based on Analytical Approximations of Band Gaps

Qiaoyun Wu[1,2], Peishan Xu[1], Zhifeng Xu[1,*], Xuyong Chen[1]

1.School of Civil Engineering and Architecture, Wuhan Institute of Technology, Wuhan, Hubei 430073
2.State Key Laboratory for Health and Safety of Bridge Structures, Wuhan, Hubei 430034
*. Corresponding author: Zhifeng Xu, 20120102@wit.edu.cn, +86-15927279709

Abstract: This research investigates band gaps and frequency responses of one-dimensional periodic structures and further presents an optimal design approach for one-dimensional rubber-concrete periodic foundations based on the proposed analytical formulas for approximating the first few band gaps. The presented design approach is optimal for being able of globally searching the best solution which effectively cooperates the band gaps with the superstructure's resonance frequencies. Firstly, frequency responses of one-dimensional periodic structures and the corresponding approximation method are studied. Furthermore, analytical approximation formulas for the first few band gaps, localization factor, attenuation coefficient, and frequency responses of one-dimensional rubber-concrete periodic foundations are proposed and verified. Lastly, inspired by the proposed analytical approximation for computing band gaps, an optimal design approach for one-dimensional rubber-concrete periodic foundations is presented and applied to a practical example, whose optimality is verified theoretically and numerically.

Keywords: Periodic foundation; Band gap; Frequency response; Vibration attenuation; Optimal design

1.INTRODUCTION

Periodic structures are obtained by repetitively arranging an identical sub-structure called unit-cell, which exhibit a unique ability to manipulate the propagation of waves according to their frequencies [1]. Theoretical study on frequency dependent properties of periodic structures can retrospect to the 1970s when Delph [2] proposed analytical solutions for harmonic wave propagating an ideal one-dimensional (1-D) periodic structure by using transfer matrix method. In the paper, it is found that the dispersion spectrum of 1-D periodic structures has a wave selecting characteristic, which hampers the energy transmission of waves belong to certain frequency intervals through reflections or refractions. On the other hand, similar conclusions can be drawn by using periodic beam models, periodic plate models, or periodic shell models [3-5]. The frequency bands that prohibit or decrease the energy transmission are refer to as band gaps (BGs) or attenuation zones [6], while harmonic waves whose frequencies outside BGs can travel through the periodic structure without any energy loss. At this junction, it is noted that perfect prohibit of wave propagation is achieve on condition that the periodic structure is ideal i.e., the number of unit-cells is infinity. Moreover, BGs seem to be a universal characteristic shared by all types of periodic structures, regardless of whether it is 1-D, two-dimensional or three-dimensional [6-12]. Sigalas and Economou [13] demonstrated that ideal 2-D cylinders embedded in matrix materials have BGs in two dimensions, which is achieved by structuring and arranging the phase or geometry of the materials. Kafesaki et al. [14] presented the existence of BGs of 3-D periodic polymer matrix composites.

The above-mentioned frequency selecting property endows periodic structures a wide application scope, ranging from light controlling [15], electronic transport manipulation [16], noise reductions [17], to seismic vibration attenuations [8,18-23]. Compared to conventional passive seismic control systems, periodic structures have the advantages of simple manufacturing and being able of mitigating responses of horizontal and vertical earthquakes simultaneously [24-26], which continues attracting scholars' interests for the recent years. Shi et al. [7] proposed the idea of using periodic structures as isolators against ground motion, in which the isolator is termed as periodic foundation. Later, different forms of periodic foundations have been rapidly developed, from 1-D to 2-D and 3-D, from simple unit-cell to multi-material complex unit-cell [9,10,12,27]. Xiang et al. [26] verified the vibration reduction effect of the BGs through a combination of the numerical simulation and experimental tests. Jia et al. [20] demonstrated the seismic attenuation effect of 1-D and 2-D periodic foundations through finite element analyses. Yan et al. [9,10] conducted experimental studies of two-dimensional and three-dimensional periodic foundations, in which the result shows periodic foundations can have satisfactory vibration reduction performances if the periodic structures are well design.

Among various periodic foundations, we are mostly interested in the 1-D rubber-concrete (RC) periodic foundations for their economy in cost, simplicity in manufacturing, as well as the potential to alleviate both pressure wave (P-wave) and shear wave (S-wave). Reasonable seismic design of periodic foundations should be based on theorical understanding of periodic structure, in which knowledge on BGs is of paramount significance. Sackman et. al. [28] proposes analytical approximation solutions for the lower bound (LB) and upper bound (UB) of the 1st BG of 1-D periodic structures. The solutions are accurate for calculating the UB of the first BG, yet the accuracy of the LB is not satisfactory for many practical cases. Zhifei et al. [29] modified Sackman's approximation solution, which is however merely a curve fitting result that can be inaccuracy for cases beyond the scope of their numerical study.

Aiming at designing optimal periodic foundations, this research studies the frequency related properties of 1-D periodic structures and further proposes an optimal design approach for 1-D RC periodic foundations. First of all, frequency responses (FRs) of one-dimensional periodic structures and the corresponding approximation method are studied. On top of that, analytical approximation formulas for the first few band gaps, localization factor (LF), attenuation coefficient (AC), and FRs of 1-D RC periodic foundations are proposed and verified. Last but not the least, inspired by the proposed analytical formulas for band gap approximations, an optimal design approach for one-dimensional rubber-concrete periodic foundations is presented and therefore implemented to designing the foundation of a 3-story steel frame, whose optimality is verified both theoretically and numerically. The paper is organized as follows: Section 2 presents the theoretical fundamentals of 1-D periodic structures; Section 3 studies the frequency responses of 1-D periodic structures, in which the FR matrix and its approximation calculations are proposed, and the superstructure-foundation coupling effect is analyzed; Section 4 proposes analytical formulas for approximating the first few BGs, LF, AC, and FRs of 1-D RC periodic foundations; Section 5 presents and validifies the optimal design approach of 1-D RC periodic foundations.

2.Theoretical fundamentals

This section reviews fundamentals of 1-D periodic structures. As shown in Fig. 1, the structure is a 1-D periodic structure that consists of n unit-cells lying along with the *y*-direction in a repetitive manner. Each unit-cell contains m elastic layers, in which the thickness of k^{th} layer is h_k, the thickness of the unit-cell is $h=\sum_{k=1}^{m} h_k$, and the total length of the entire periodic structure is $H=nh$. The structure is ideal if $n=\infty$. The local coordinate of the k^{th} layer in the j^{th} unit-cell is related to the global coordinate by $y=(j-1)h+\sum_{p=0}^{k-1} h_p + y_{j,k}$, where y is the global coordinate and $y_{j,k}$ is the local coordinate of the layer. For the k^{th} layer, the Young's, Poisson's ratio and density are respectively E_k, υ_k, and ρ_k. Displacement, velocity, acceleration and stress component of the structure and the corresponding quantities of the layer are linked by $u(y)=u_{j,k}(y_{j,k})$, $v(y)=v_{j,k}(y_{j,k})$, $a(y)=a_{j,k}(y_{j,k})$, $\sigma(y)=\sigma_{j,k}(y_{j,k})$. The bottom and the top are characterized by $y=0$ and $y=H$ respectively. Incident waves with different frequency can be input at the bottom in *x*-direction or *y*-direction, representing S-waves or P-waves respectively. For S-waves, $u(y)$, $v(y)$ and $a(y)$ are in the *x*-direction, and $\sigma(y)$ is shear stress. For P-waves, $u(y)$, $v(y)$ and $a(y)$ are in the *y*-direction, and $\sigma(y)$ is normal stress.

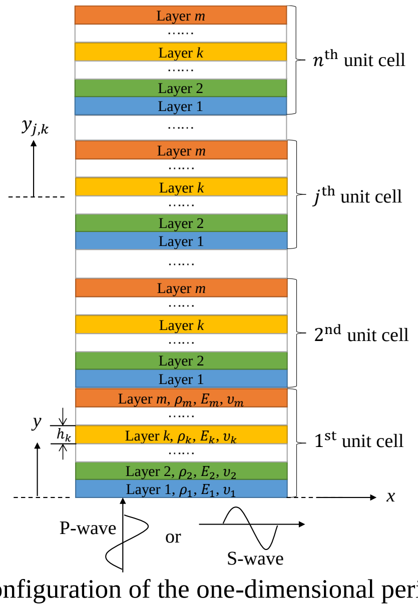

FIGURE 1 Configuration of the one-dimensional periodic structure.

The governing equation for an elastic wave propagating through the k^{th} layer in the j^{th} unit-cell can be described by the follow wave equation:

$$\frac{\partial^2 u_{j,k}(y_{j,k},t)}{\partial t^2} = c_k{}^2 \frac{\partial^2 u_{j,k}(y_{j,k},t)}{\partial y_{j,k}{}^2} \tag{1}$$

where $c_k = \sqrt{\frac{\kappa_k}{\rho_k}}$ is the phase velocity. For S-waves, $\kappa_k = \mu_k$, for P-waves, $\kappa_k = \lambda_k + 2\mu_k$, $\mu_k = \frac{E_k}{2(1+\upsilon_k)}$ and $\lambda_k = \frac{\upsilon_k E_k}{(1+\upsilon_k)(1-2\upsilon_k)}$ are the Lamé constants.

The particular solution with respect to a harmonic excitation satisfies the following separable form:

$$u_{j,k,l}\left(y_{j,k},t\right) = \exp\left(\mathrm{i}\omega_l t\right) U_{j,k,l}\left(y_{j,k}\right) \tag{2}$$

$$U_{j,k,l}\left(y_{j,k}\right) = A_{j,k,l}\sin\left(k_{k,l} y_{j,k}\right) + B_{j,k,l}\cos\left(k_{k,l} y_{j,k}\right) \tag{3}$$

where t represent time, ω_l is frequency, $k_{k,l} = \frac{\omega_l}{c_k}$ is the wave number, and i is the imaginary unit.

According to Hooke's low, the stress component is

$$\sigma_{j,k,l}\left(y_{j,k},t\right) = \frac{\partial u_{j,k,l}\left(y_{j,k},t\right)}{\partial y_{j,k}} = \exp\left(\mathrm{i}\omega_l t\right)\Sigma_{j,k,l}\left(y_{j,k}\right) \tag{4}$$

in which

$$\Sigma_{j,k,l}\left(y_{j,k}\right) = \kappa_k k_{k,l}\left[A_{j,k,l}\sin\left(k_{k,l}y_{j,k}\right) - B_{j,k,l}\cos\left(k_{k,l}y_{j,k}\right)\right] \tag{5}$$

The general solution of Eq. (1) with respective to an arbitrary excitation can be written as the superposition of each particular solution, i.e., $u_{j,k}\left(y_{j,k},t\right) = \int s(\omega_l)\exp\left(\mathrm{i}\omega_l t\right)U_{j,k,l}\left(y_{j,k}\right)\mathrm{d}\omega_l$, in which $s(\omega_l)$ is the Fourier component that determined by matching the initial and boundary conditions. And the general solution degenerated into the particular solution described by Eq. (2) if the excitation is a harmonic wave.

2.1 Transfer-matrix method

Now we focus on the cases of harmonic waves. By using the transfer matrix method, Eq. (3) and Eq. (5) can be rearranged into the following matrix multiplication form:

$$\mathbf{W}_{j,k,l}\left(y_{j,k}\right) = \mathbf{H}_{j,k,l}\left(y_{j,k}\right)\mathbf{\Psi}_{j,k,l} \tag{6}$$

where $\mathbf{W}_{j,k,l}\left(y_{j,k}\right) = \begin{bmatrix} U_{j,k,l}\left(y_{j,k}\right) \\ \Sigma_{j,k,l}\left(y_{j,k}\right) \end{bmatrix}$ is the state vector, $\mathbf{\Psi}_{j,k,l} = \begin{bmatrix} A_{j,k,l} \\ B_{j,k,l} \end{bmatrix}$ is a constant vector, and

$$\mathbf{H}_{j,k,l}\left(y_{j,k}\right) = \begin{bmatrix} \sin\left(k_{k,l}y_{j,k}\right) & \cos\left(k_{k,l}y_{j,k}\right) \\ \kappa_k k_{k,l}\cos\left(k_{k,l}y_{j,k}\right) & -\kappa_k k_{k,l}\sin\left(k_{k,l}y_{j,k}\right) \end{bmatrix} \tag{7}$$

Substituting $y_{j,k} = 0$ and $y_{j,k} = h_k$ into Eq. (6) yields:

$$\mathbf{W}_{j,k,l}\left(h_k\right) = \mathbf{T}_{k,l}\left(h_k\right)\mathbf{W}_{j,k,l}\left(0\right) \tag{8}$$

in which the following transfer matrix of the layer is defined by

$$\mathbf{T}_{k,l}\left(h_k\right) = \mathbf{H}_{j,k,l}\left(h_k\right)\left[\mathbf{H}_{j,k,l}\left(0\right)\right]^{-1} \tag{9}$$

By substituting Eq. (7) into Eq. (9), the explicit form of layer's transfer matrix is obtained as

$$\mathbf{T}_{k,l}\left(h_k\right) = \begin{bmatrix} \cos\left(k_{k,l}h_k\right) & \frac{1}{\kappa_k k_{k,l}}\sin\left(k_{k,l}h_k\right) \\ -\kappa_k k_{k,l}\sin\left(k_{k,l}h_k\right) & \cos\left(k_{k,l}h_k\right) \end{bmatrix} \tag{10}$$

It is noted that the determinant $\left|\mathbf{T}_{k,l}\left(h_k\right)\right| = 1$.

By using the continuity condition between layers, i.e., $\mathbf{W}_{j,k+1,l}\left(0\right) = \mathbf{W}_{j,k+1,l}\left(h_k\right)$, the relation between the top and bottom of the j^{th} unit-cell is achieved by the following recursive expression:

$$\mathbf{W}_{j,l}\left(h\right) = \mathbf{W}_{j,m,l}\left(h_m\right) = \mathbf{T}_{m,l}\left(h_k\right)\mathbf{W}_{j,m,l}\left(0\right) = \cdots = \mathbf{T}\left(h\right)\mathbf{W}_{j,l}\left(0\right) \tag{11}$$

where $\mathbf{T}_l\left(h\right) = \prod_{k=1}^{m}\mathbf{T}_{k,l}\left(h_k\right)$ is the transfer matrix of the unit-cell. Since $\left|\mathbf{T}_{k,l}\left(h_k\right)\right| = 1$, it can be obtained that the determinant $\left|\mathbf{T}_l\left(h_k\right)\right| = 1$.

Similarly, the translation relation between the top and bottom of the 1-D periodic structure is

$$\mathbf{W}(H) = \mathbf{W}_{n,l}(h) = \mathbf{T}_l(h)\mathbf{W}_{n,l}(0) = \cdots = \left[\mathbf{T}_l(h)\right]^n \mathbf{W}_{1,l}(0) = \mathbf{T}_l^n \mathbf{W}(0) \tag{12}$$

where $\mathbf{T}_l^n = \left[\mathbf{T}_l(h)\right]^n$ is the transfer matrix of the entire structure.

And the backward transfer relation is

$$\mathbf{W}(0) = \mathbf{W}_{1,l}(0) = \mathbf{T}_l(h)^{-1} \mathbf{W}_{1,l}(h) = \cdots = \left[\mathbf{T}_l(h)^{-1}\right]^n \mathbf{W}(H) = \left[\mathbf{T}_l^n\right]^{-1} \mathbf{W}(H) \tag{13}$$

where $\mathbf{T}_l(h)^{-1}$ and $\left[\mathbf{T}_l^n\right]^{-1}$ are the inverse matrices of $\mathbf{T}_l(h)$ and $\mathbf{T}_l^n$ respectively.

2.2 Band gaps

Based on the Floquet-Bloch theory, the state vectors of top and bottom of a unit-cell have the following relation:

$$\mathbf{W}_{j,l}^{\Lambda}(h) = \exp(\mathrm{i}kh)\mathbf{W}_{j,l}^{\Lambda}(0) \tag{14}$$

in which k is the wave number of the unit-cell, $\mathbf{W}_{j,l}^{\Lambda}(h)$ and $\mathbf{W}_{j,l}^{\Lambda}(0)$ are the state vectors in the complex eigen-modes.

Substituting Eq. (14) into Eq. (11), the following eigen-form equation is obtained:

$$\left[\mathbf{T}_l(h) - \exp(\mathrm{i}kh)\mathbf{I}\right]\mathbf{W}_{j,l}^{\Lambda}(0) = \mathbf{0} \tag{15}$$

in which $\mathbf{I}$ is the identity matrix, the two eigen-vectors are $\mathbf{W}_{j,l}^{\Lambda_1}(0)$ and $\mathbf{W}_{j,l}^{\Lambda_2}(0)$, the two eigen-values are $\Lambda_1 = \exp(\mathrm{i}k_1 h)$ and $\Lambda_2 = \exp(\mathrm{i}k_2 h)$ satisfying

$$\left|\mathbf{T}_l(h) - \exp(\mathrm{i}k_{1\text{ or }2}h)\mathbf{I}\right| = 0 \tag{16}$$

The solution of Eq. (16) is

$$\exp(\mathrm{i}k_{1\text{ or }2}h) = \Lambda_{1\text{ or }2} = \frac{\mathrm{trace}\left[\mathbf{T}_l(h)\right] \pm \sqrt{\mathrm{trace}\left[\mathbf{T}_l(h)\right]^2 - 4}}{2} \tag{17}$$

where $\mathrm{trace}\left[\mathbf{T}_l(h)\right] = \mathrm{T}_{l11}(h) + \mathrm{T}_{l22}(h)$.

Eq. (16) implies the following conditions are valid:

$$\exp(\mathrm{i}k_1 h) + \exp(\mathrm{i}k_2 h) = \mathrm{trace}\left[\mathbf{T}_l(h)\right] \tag{18}$$

$$\exp(\mathrm{i}k_1 h)\exp(\mathrm{i}k_2 h) = \exp\left[\mathrm{i}\left(k_1 + k_2\right)h\right] = \left|\mathbf{T}_l(h)\right| = 1 \tag{19}$$

Behaviors of the state vectors can be classified into the following two cases: (a) no attenuation case, $\left|\mathrm{T}_{l11}(h) + \mathrm{T}_{l22}(h)\right| < 2$, Λ_1 and Λ_2 forms a pair of conjugates, i.e., $\Lambda_{1,2} = \Lambda_{\mathrm{re}} \pm \mathrm{i}\Lambda_{\mathrm{im}}$, $\left|\Lambda_{1,2}\right| = 1$, k_1 and k_2 are two real numbers satisfying $k_1 + k_2 = 0$. In this case, the state vectors will only keep elliptically rotating so that waves can travel through without any energy loss. (b) attenuation case, $\left|\mathrm{T}_{l11}(h) + \mathrm{T}_{l22}(h)\right| > 2$, Λ_1 and Λ_2 are two real numbers $\Lambda_1\Lambda_2 = 1$, $\left|\Lambda_1\right| < 1 < \left|\Lambda_2\right|$, k_1 and k_2 become two complex numbers. According to the eigen-value power method, given an arbitrary $\mathbf{W}(h)$, $\mathbf{W}(0)$ will be eventually attracted to the eigen direction of $\mathbf{T}_l(h)^{-1}$, which is identical to the direction of $\mathbf{W}_{j,l}^{\Lambda_1}(0)$, as n increases. And each increase of n by 1 will approximately magnify $\left|\mathbf{W}(0)\right|$ by $\left|\Lambda_1^{-1}\right| = \dfrac{1}{\left|\Lambda_1\right|}$. Consequently, if we track the wave propagation from bottom to top, the wave amplitude is decayed per unit-cell at a constant rate referred to as the AC, i.e.:

$$r = 1 - \Lambda_1 = 1 - \exp(-\gamma) \tag{20}$$

where $\gamma = -\ln\left|\Lambda_1\right|$ is the LF. Obviously, after travelling through the entire periodic structure, the wave amplitude is decayed by $r = 1 - \exp(-n\gamma)$. And frequencies in this case form the BGs (attenuation zones) consequently. Figs. 2 show the behaviors of the state vectors of the benchmark unit-cells defined by Table 1, from which the phenomena of above discussed two cases can be observed. For ideal 1-D periodic structures, since $n \to \infty$, the amplitude of the output wave becomes $\lim_{n\to\infty}\exp(-n\gamma) = 0$, which means wave propagations are prohibited. Figs. 3 (a) and (b) show the dispersion curves (p.s., wave number VS frequency) of the benchmark unit-cell described by Table 1 undergoing S-waves or P-waves respectively. And the LF and AC are shown in Figs. 4 (a) and (b) respectively, from which it is seen that the attenuation effect of each BG is monotonically increasing with the increase of n.

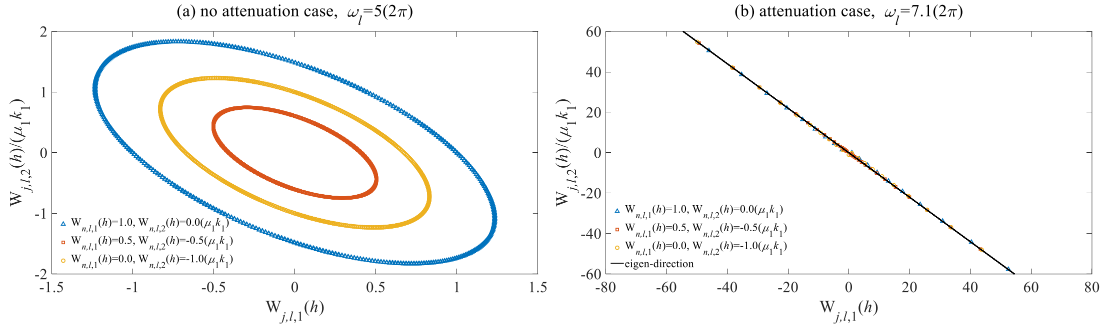

FIGURE 2 Behaviors of unit cells' state vectors: (a) no attenuation case, (b) attenuation case.

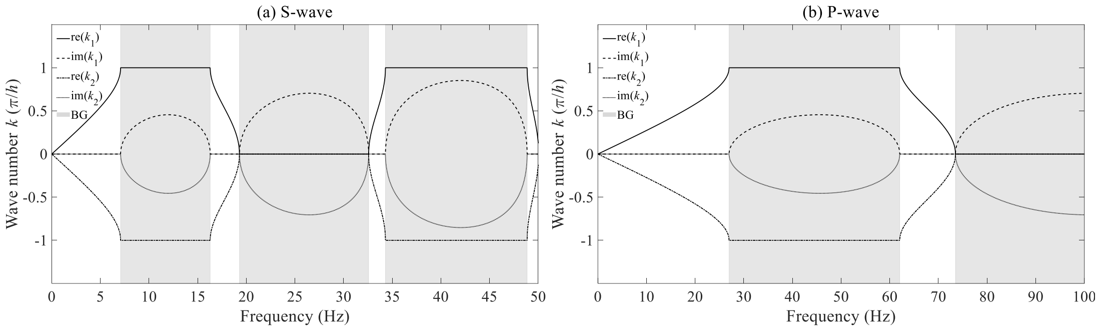

FIGURE 3 Dispersion curves of the 1-D periodic structure: (a) S-wave, (b) P-wave.

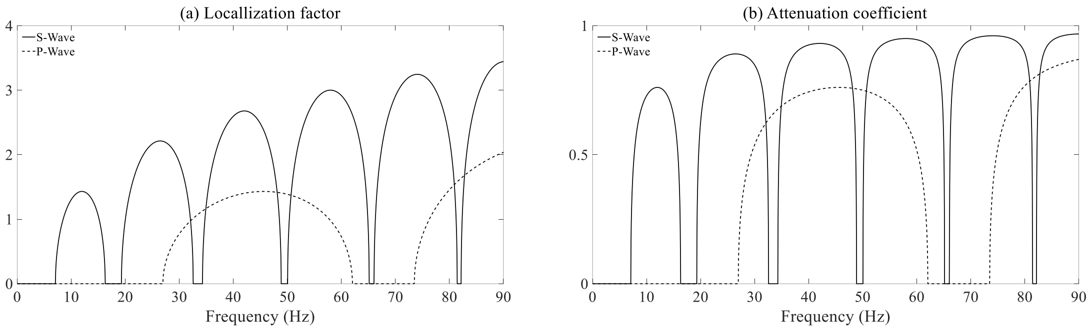

FIGURE 4 Localization factor and attenuation coefficient of the unit-cell.

TABLE 1 Configuration of the benchmark unit-cell

layer label	material	Young's modulus (MPa)	density (kg/m^3)	Poisson's ratio	layer thickness (m)
1	rubber	0.1586	1277	0.463	0.2
2	concrete	40,000	2300	0.2	0.2

3.FREQUENCY RESPONSES OF ONE-DIMENSIONAL PERIODIC STRUCTURES

FR is the core measure of vibration attenuation performance in seismic engineering, which is usually express as the absolute ratio of nominal amplitude of the input to nominal amplitude of the corresponding output as a function of frequency. This sections studies FRs of 1-D periodic structures, in which the analytical form of FR matrix and the corresponding approximations are proposed and verified, and superstructure-foundation coupling effect is further investigated.

3.1 Frequency response matrix

Firstly, the following FR matrix is defined:

$$\mathbf{FR} = \begin{bmatrix} \left|\dfrac{W_1(H)}{W_1(0)}\right| & \left|\dfrac{W_1(H)}{W_2(0)}\right| \\ \left|\dfrac{W_2(H)}{W_1(0)}\right| & \left|\dfrac{W_2(H)}{W_2(0)}\right| \end{bmatrix} \tag{21}$$

where the numeric subscript represents the corresponding component of the vector or matrix, $\mathrm{FR}_{11}=\left|\frac{\mathrm{W}_1(H)}{\mathrm{W}_1(0)}\right|=\left|\frac{\sigma(H)}{\sigma(0)}\right|$ is the FR of displacement, $\mathrm{FR}_{12}=\left|\frac{\mathrm{W}_1(H)}{\mathrm{W}_2(0)}\right|=\left|\frac{u(H)}{\sigma(0)}\right|$ is the FR of displacement to traction, $\mathrm{FR}_{21}=\left|\frac{\mathrm{W}_2(H)}{\mathrm{W}_1(0)}\right|=\left|\frac{\sigma(H)}{u(0)}\right|$ is the FR of traction to displacement, $\mathrm{FR}_{22}=\left|\frac{\mathrm{W}_2(H)}{\mathrm{W}_2(0)}\right|=\left|\frac{\sigma(H)}{\sigma(0)}\right|$ is the FR of stress or traction. In practice, it is convenient to use the frequency response function (FRF) instead of FR, i.e., $\mathbf{FRF}=20\log_{10}\mathbf{FR}$.

Substituting Eq. (12) into Eq. (21) yields the following analytical form of FR matrix

$$\mathbf{FR}=\begin{bmatrix}\left|\mathrm{T}_{l11}^{n}+\mathrm{T}_{l12}^{n}\frac{\mathrm{W}_2(0)}{\mathrm{W}_1(0)}\right| & \left|\mathrm{T}_{l12}^{n}+\mathrm{T}_{l11}^{n}\frac{\mathrm{W}_1(0)}{\mathrm{W}_2(0)}\right| \\ \left|\mathrm{T}_{l21}^{n}+\mathrm{T}_{l22}^{n}\frac{\mathrm{W}_2(0)}{\mathrm{W}_1(0)}\right| & \left|\mathrm{T}_{l22}^{n}+\mathrm{T}_{l21}^{n}\frac{\mathrm{W}_1(0)}{\mathrm{W}_2(0)}\right|\end{bmatrix} \tag{22}$$

If the top surface of the periodic structure is free, i.e., $\mathrm{W}_2(H)=0$, Eq. (22) becomes

$$\mathbf{FR}_{\mathrm{free}}=\begin{bmatrix}\left|\frac{1}{\mathrm{T}_{l22}^{n}}\right| & \left|\frac{1}{\mathrm{T}_{l21}^{n}}\right| \\ 0 & 0\end{bmatrix} \tag{23}$$

If the top surface is clamped, i.e., $\mathrm{W}_1(H)=0$, then Eq. (22) becomes

$$\mathbf{FR}_{\mathrm{clamped}}=\begin{bmatrix}0 & 0 \\ \left|\frac{1}{\mathrm{T}_{l12}^{n}}\right| & \left|\frac{1}{\mathrm{T}_{l11}^{n}}\right|\end{bmatrix} \tag{24}$$

3.2 Frequency response approximation

As introduced in Section 2, if the frequency of incident wave belongs the BGs, the incident wave $\mathbf{W}(0)$ is always close to the eigen-model, and the amplitude of the incident wave is approximated decreased by r. Thus, if n is sufficiently large, Eq. (22) can be approximated as:

$$\mathbf{FR}\approx\begin{bmatrix}\left|\mathrm{T}_{l11}^{n}+\mathrm{T}_{l12}^{n}\tan\phi\right| & \left|\mathrm{T}_{l12}^{n}+\mathrm{T}_{l11}^{n}\cot\phi\right| \\ \left|\mathrm{T}_{l21}^{n}+\mathrm{T}_{l22}^{n}\tan\phi\right| & \left|\mathrm{T}_{l22}^{n}+\mathrm{T}_{l21}^{n}\cot\phi\right|\end{bmatrix}\approx(1-r)^{n}\begin{bmatrix}\left|\cos\theta\right| & \left|\sin\theta\tan\phi\right| \\ \left|\sin\theta\tan\phi\right| & \left|\cos\theta\right|\end{bmatrix} \tag{25}$$

where $\phi=\arctan\frac{\mathrm{W}_2^{\Lambda_1}(0)}{\mathrm{W}_1^{\Lambda_1}(0)}$ is the angle of the eigen-vector, and $\theta=\arctan\frac{\mathrm{W}_2(H)}{\mathrm{W}_1(H)}$. Figs. 5 show the frequency responses of the benchmark periodic structure (a 1-D periodic structure consists of benchmark unit-cells defined by Table 1) with a free or a clamped top surface undergoing S-waves or P-waves, from which the following conclusions on FRs are drawn or asserted: 1, if n is sufficiently large (e.g., n=4 for the case free top surface or n=16 for the case of clamped top surface), FRs can be well approximated by Eq. (25); 2, singularities of for FR_{21} and FR_{22} exist in the BGs when $\phi=\frac{\pi}{2}$ (i.e., $\mathrm{T}_{l21}=0$); 3, since free surface and clamped surface represent the two limiting cases, it is asserted that BGs will consistently attenuate incident waves regardless of the boundary condition of top surface.

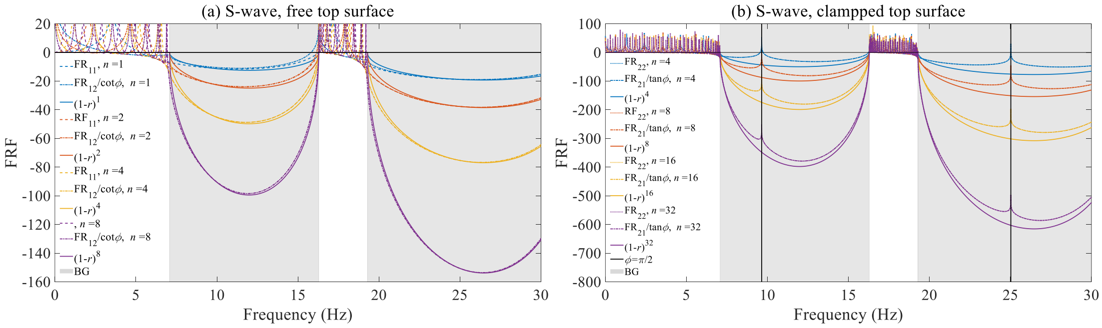

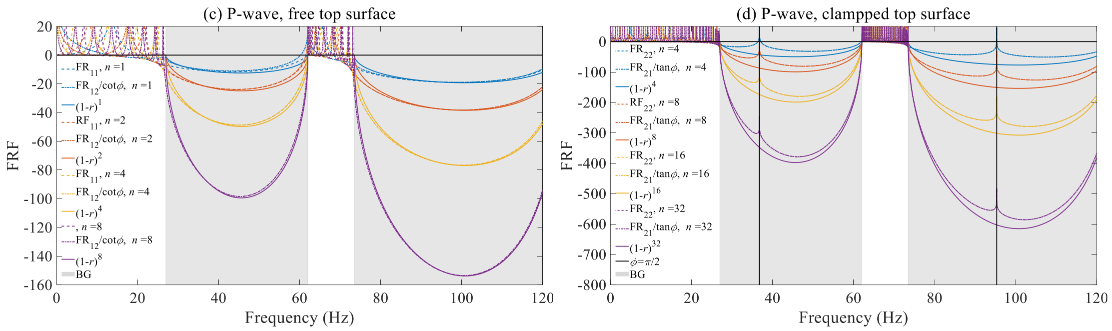

FIGURE 5 Frequency responses and their approximations: (a) S-wave, free top surface, (b) S-wave, clamped top surface, (c) P-wave, free top surface, (d) P-wave, clamped top surface.

3.3 Superstructure-foundation coupling effect

The superstructure-foundation coupling effect is tricky because of interferences between the superstructure and the foundation. A good practice for dealing with this question is modeling the superstructure as another layer above the periodic foundation [30]. Nevertheless, for qualitative study, it is sufficient to treat the influence of superstructure to foundation as a boundary condition of the top surface, in which a traction free top surface represents the limiting case of very small structures, and a clamped top surface represents the limiting case of giant structures. On that account, by treating the FRs of the foundation's top surface as the input of the superstructure and assuming $\mathbf{W}(0)$ is along with the eigen direction, the displacement FR of the entire superstructure-foundation coupled system can be approximated as

$$\left|\frac{u_{out}}{u(0)}\right| = \left|\frac{u_{out}}{u(H)}\frac{u(H)}{u(0)}\right| = \left|\frac{u_{out}}{u(h)}\right| \mathrm{FR}_{11} \approx \left|\frac{u_{out}}{u(h)}\right| (1-r)^n \left|\cos\theta\right| \tag{26}$$

In order to verify the above analysis on FRs, a finite element method (FEM) analysis using ABABQUS 6.14 was performed. In the analysis, two FEM models were built, in which one of them was the benchmark periodic foundation (shown in Fig. 6 (a)), the other was the identical foundation with a four-story steel frame described by Table 2 (shown in Fig. 6 (b)). For the foundation, the normal section was a square with a side length equals 10 m, the mesh grid size along the transversal surface and the longitude direction equals were 0.5 m and 0.05 m respectively, and the element type is C3D8. The steel frame is modeled by B33 elements. Unit harmonic displacements of different frequency were uniformly assigned to the bottom surface, in which displacements along the x-axis or y-axis represents S-waves or P-waves respectively. The "SteadyStateDirectStep" is adopted to compute the FRs, in which the frequency ranges from 0.05 to 20.0 Hz and 0.2 to 80.0 Hz for S-Waves and P-waves respectively. Figs. 7 present the comparison between the FEM simulation result of the averaged displacement FR of the four nodes connecting the superstructure to the foundation and the corresponding analytical results from Eq. (23) and Eq. (25), in which the good match between them validates the above analysis on FR. Additionally, it is concluded that, even though the superstructure-foundation coupling effect can slightly alter the FRs of the top surface, BGs consistently hamper wave propagations regardless of the existence of superstructure. This fact suggests that the superstructure-foundation coupling effect can be ignored in computing BGs.

TABLE 2 Configuration of the steel frame

geometry	number of stories	4
	length (m)	3
	width (m)	3
	story height (m)	3
	cross-section of beams (m)	0.05 by 0.05 rectangle
	cross-section of columns (m)	0.05 by 0.05 rectangle
material	Young's modulus (MPa)	200000.0
	Poisson's ratio	0.3
	density (kg/m^3)	7850

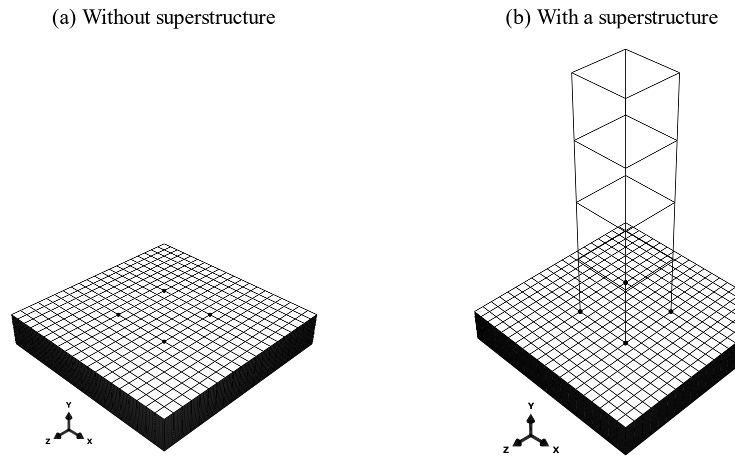

FIGURE 6 Configurations of the FEM models: (a) without superstructure, (b) with a superstructure.

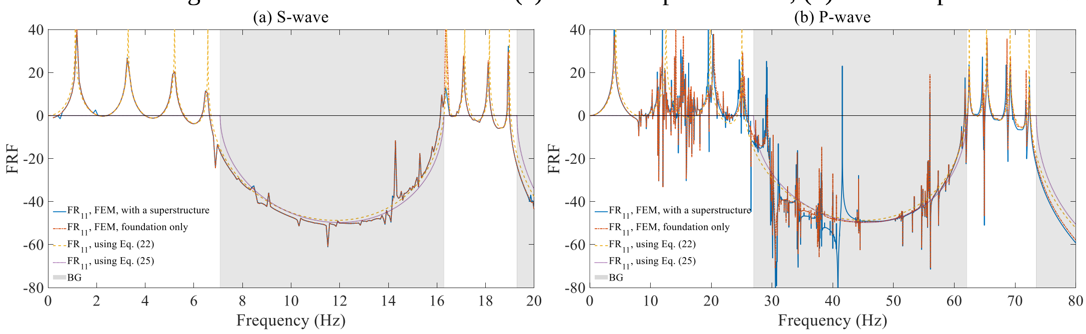

FIGURE 7 Comparison on frequency responses of the top surface: (a) S-wave, (b) P-wave.

4.STUDY ON ONE-DIMENSIONAL RUBBER-CONCRETE PERIODIC FOUNDATIONS

In this section, the analytical formulas for approximating the first few BGs, LF, AC and FRs of 1-D RC periodic structures are proposed and verified, in which the 1-D RC periodic foundation is a 1-D periodic structure whose unit cells consist of a rubber layer and a concrete layer. Besides, a one-to-one mapping relation between frequency points of BGs is established. At this point, it is defined that layer 1 is the rubber layer and layer 2 is the concrete layer.

4.1 Approximations of the first few BGs

For a 1-D RC periodic foundation, Eq. (18) can be rewritten as:

$$\mathrm{trace} = \Lambda_1 + \frac{1}{\Lambda_1} = 2\cos\left(\frac{h_1}{c_1}\omega_l\right)\cos\left(\frac{h_2}{c_2}\omega_l\right) - 2D\sin\left(\frac{h_1}{c_1}\omega_l\right)\sin\left(\frac{h_2}{c_2}\omega_l\right) \tag{27}$$

where $D = \frac{1}{2}\left(\frac{c_1\kappa_2}{c_2\kappa_1} + \frac{c_2\kappa_1}{c_1\kappa_2}\right)$. Besides, the symmetry of Eq. (27) with respect to the superscripts indicates the order of the two layers is trivial in the computation of BGs.

The boundaries of BGs are characterized by $\Lambda_1 = \pm 1$. Meanwhile, if $\frac{h_2}{c_2} \ll \frac{h_1}{c_1}$ and ω_l is small, which is nearly universal for anti-seismic consideration of 1-D RC periodic foundations, it is guaranteed that $\cos\left(\frac{h_2}{c_2}\omega_l\right) \approx 1$, $\sin\left(\frac{h_2}{c_2}\omega_l\right) \approx \frac{h_2}{c_2}\omega_l$, then Eq. (27) becomes

$$\cos\left(\frac{h_1}{c_1}\omega_l\right) - D\frac{h_2}{c_2}\omega_l \sin\left(\frac{h_1}{c_1}\omega_l\right) = \pm 1 \tag{28}$$

The solution of Eq. (28) provides approximations of the lower bounds (LBs) and upper bounds (UBs) of the first few BGs, which can be further expressed as the following form:

$$\cos\left(\frac{h_1}{c_1}\omega_l + \theta\right) \approx \cos\left(\pm\theta + p\pi\right) \tag{29}$$

where $\theta = \arctan\left(D\omega_l h_2 / c_2\right)$, and p is a non-negative integer.

$h_1\omega_l / c_1 + \theta \approx \theta + p\pi$ marks the UBs of the first few BGs, i.e.:

$$\omega_{p-\text{end}} \approx p\pi \frac{c_1}{h_1} \tag{30}$$

It is noted that $\omega_{1-\text{end}} \approx \pi c_1 / h_1$ is identical with Sackman's approximation [28].

On the other hand, the LBs are marked by $\frac{h_1}{c_1}\omega_l + \theta \approx -\theta + p\pi$, i.e., $\frac{1}{2}\frac{h_1}{c_1}\omega_l + p\pi \approx -\theta$ or $\frac{1}{2}\frac{h_1}{c_1}\omega_l + p\pi \approx \frac{1}{2}\pi - \theta$. Since $\tan(-\theta) \approx -D\frac{h_2}{c_2}\omega_l$ and $\cot(\frac{\pi}{2} - \theta) \approx D\frac{h_2}{c_2}\omega_l$ hold, by using $\cot(-\theta) \approx -\frac{c_2}{Dh_2\omega_l}$ and $\tan(\frac{\pi}{2} - \theta) \approx \frac{c_2}{Dh_2\omega_l}$, the following two equations are obtained as the implicit approximations for the LBs of BGs:

$$\cot(\frac{1}{2}\frac{h_1}{c_1}\omega_l + p\pi) + \frac{c_2}{Dh_2\omega_l} \approx 0 \tag{31}$$

$$\tan(\frac{1}{2}\frac{h_1}{c_1}\omega_l + p\pi) - \frac{c_2}{Dh_2\omega_l} \approx 0 \tag{32}$$

To further obtain an explicit approximation for the LBs of the first few BGs, substituting $\tan(\frac{1}{2}\frac{h_1}{c_1}\omega_l + p\pi) \approx \frac{1}{2}\frac{h_1}{c_1}\omega_l + p\pi$ and $\cot(\frac{1}{2}\frac{h_1}{c_1}\omega_l + p\pi) \approx \frac{\pi}{2} - \frac{1}{2}\frac{h_1}{c_1}\omega_l + p\pi$ into Eq. (31) and Eq. (32) respectively and combining the results yields

$$\omega_{p-\text{start}} = \frac{c_1}{h_1}\left[\frac{p-1}{2}\pi + \sqrt{\left(\frac{p-1}{2}\pi\right)^2 + \frac{2c_2h_1}{Dc_1h_2}}\right] \tag{33}$$

In order to verify to proposed approximation formulas, the exact values of BGs of the benchmark unit-cell computed by Eq. (27) and the corresponding approximations using Eq. (30) to Eq. (33) are presented and compared in Figs. 8 and Table 3 in terms of frequency rather than angular frequency. It can be seen that, except for the relative conservative approximation of $\omega_{1-\text{start}}$ using Eq. (33), the rest approximations all have sufficient accuracy.

TABLE 3 Lower bounds and upper bounds of the first few band gaps

frequency	S-wave					P-wave				
	Eq. (27)	Eq. (30)	Eq. (31)	Eq. (32)	Eq. (33)	Eq. (27)	Eq. (30)	Eq. (31)	Eq. (32)	Eq. (33)
$f_{1\text{-start}}$ (Hz)	7.078	-	7.078	-	7.726	26.970	-	26.970	-	29.434
$f_{1\text{-end}}$ (Hz)	16.286	16.287	-	-	-	62.049	62.050	-	-	-
$f_{2\text{-start}}$ (Hz)	19.294	-	-	19.2940	19.369	73.504	-	-	73.504	73.791
$f_{2\text{-end}}$ (Hz)	32.574	32.575	-	-	-	124.098	124.101	-	-	-
$f_{3\text{-start}}$ (Hz)	34.298	-	34.298	-	34.315	130.669	-	130.669	-	130.728
$f_{3\text{-end}}$ (Hz)	48.862	48.863	-	-	-	186.148	186.151	-	-	-
$f_{4\text{-start}}$ (Hz)	50.050	-	-	50.0500	50.055	190.674	-	-	190.674	190.694
$f_{4\text{-end}}$ (Hz)	65.150	65.150	65.150	-	-	248.197	248.202	-	-	-
$f_{5\text{-start}}$ (Hz)	66.052	-	66.052	-	66.0544	251.634	-	251.634	-	251.644
$f_{5\text{-end}}$ (Hz)	81.438	81.438	-	-	-	310.246	310.252	-	-	-

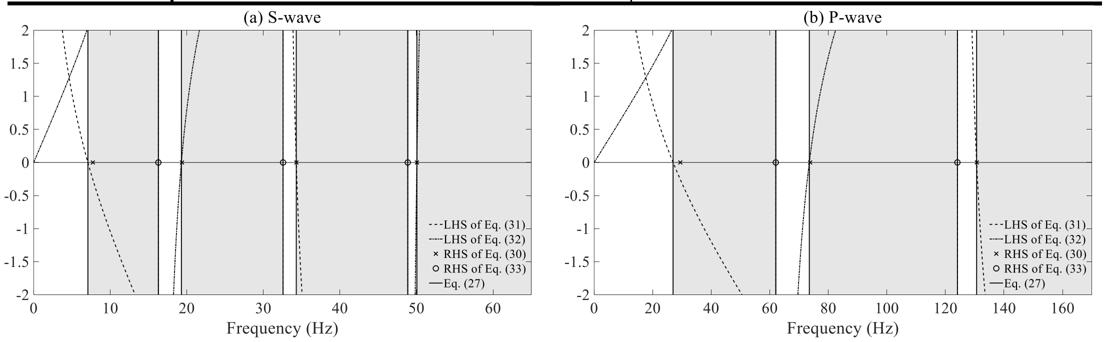

FIGURE 8 Approximations of the first few bad gaps: (a) S-wave, (b) P-wave.

4.2 Mapping relations of band gaps

From Eq. (30), it is apparent that the ending points of BGs form an arithmetic sequence. At this junction, the increment of this arithmetic sequence is defined as band interval (BI), i.e. $\mathrm{BI} = \pi \frac{c_1}{h_1}$, which is solely determine by the properties of the rubber layer. Besides, the ratio of BI for S-wave to BI for P-Waves is the following constant referred to as the mapping ratio (MR), i.e.:

$$\mathrm{MR} = \frac{\mathrm{BI_S}}{\mathrm{BI_P}} = \sqrt{\frac{\mu_1}{\lambda_1 + 2\mu_1}} = \sqrt{\frac{1-2\upsilon_1}{2(1-\upsilon_1)}} \tag{34}$$

in which the subscripts 'S' and 'P' represent S-Wave and P-Wave respectively.
The occupation rate (OR) of the p^{th} BG is defined as the ratio of BG's width to BI, i.e.:

$$o_p = \frac{\omega_{p-\text{end}} - \omega_{p-\text{start}}}{\mathrm{BI}} \tag{35}$$

Consequently, the LB and UB of p^{th} BG are $\omega_{p-\text{start}} = (p - o_p)\mathrm{BI}$ and $\omega_{p-\text{start}} = p\mathrm{BI}$. Substituting Eq. (30) and $D = \frac{1}{2}\left(\frac{c_1\kappa_2}{c_2\kappa_1} + \frac{c_2\kappa_1}{c_1\kappa_2}\right)$ into Eq. (33) yields

$$o_p \approx \frac{p+1}{2} - \sqrt{\left(\frac{p-1}{2}\right)^2 + \frac{4h_1}{\pi^2\left(\frac{\rho_2}{\rho_1} + \frac{\kappa_1}{\kappa_2}\right)h_2}} \approx \frac{p+1}{2} - \sqrt{\left(\frac{p-1}{2}\right)^2 + \frac{4h_1\rho_1}{\pi^2 h_2\rho_2}} \tag{36}$$

in which $\kappa_1/\kappa_2 \approx 0$ is used for the second approximation. Eq. (36) indicates ORs for S-waves and for P-waves are nearly identical. And it can be concluded that: 1, $\frac{\omega_{p-\text{start}-\text{S}}}{\omega_{p-\text{start}-\text{P}}} = \frac{\omega_{p-\text{end}-\text{S}}}{\omega_{p-\text{end}-\text{P}}} = \mathrm{MR}$; 2, $\frac{\mathrm{d}o_p}{\mathrm{d}p} \approx \frac{\sqrt{\left(\frac{p-1}{2}\right)^2 + \frac{4h_1\rho_1}{\pi^2 h_2\rho_2}} - \left(\frac{p-1}{2}\right)}{2\sqrt{\left(\frac{p-1}{2}\right)^2 + \frac{4h_1\rho_1}{\pi^2 h_2\rho_2}}} > 0$; 3, $\lim_{p\to\infty} o_p \approx \lim_{p\to\infty} \frac{p - \frac{4h_1\rho_1}{\pi^2 h_2\rho_2}}{\frac{p+1}{2} + \sqrt{\left(\frac{p-1}{2}\right)^2 + \frac{4h_1\rho_1}{\pi^2 h_2\rho_2}}} = 1$; 4, o_p is monotonic increasing with h_2/h_1 or ρ_2/ρ_1. Fig. 9 shows comparison between the exact value of o_p and the approximation through Eq. (36) using the benchmark unit-cell, in which the close match between them demonstrates the validity of Eq. (36).

In addition, the following one-to-one mapping relations are concluded:

1. A frequency point of the p^{th} BG can be mapped to a frequency point of the q^{th} BG by

$$\omega_{l-p} = (p - \Delta o_p)\mathrm{BI} \to \omega_{l-q} = (q - \Delta o_q)\mathrm{BI} \tag{37}$$

where $0 \le \Delta \le 1$ is the BG's local coordinate pointing to negative infinity.

2. A frequency point for S-waves can be mapped to the corresponding point for P-waves by

$$\omega_{l-\text{S}} = \mathrm{MR}\,\omega_{l-\text{P}} \tag{38}$$

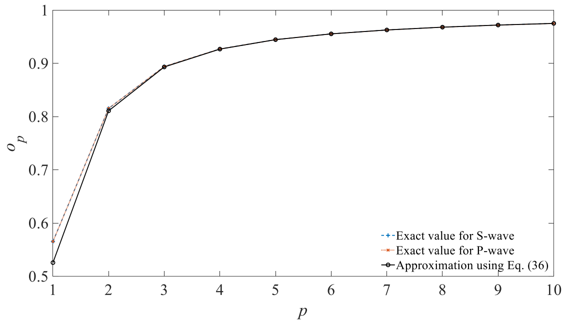

FIGURE 9 Comparison between the exact values and the approximations for occupation rates.

4.3 Approximations of first band gap

According to Eq. (30), the BIs and the UB of the 1st BG for S-wave and P-wave are

$$\mathrm{BI_S} = \omega_{1-\text{end}-\text{S}} \approx \pi\sqrt{\frac{E_1}{2(1+\upsilon_1)\rho_1 h_1^2}} \tag{39}$$

$$\mathrm{BI_P} = \omega_{1-\mathrm{end-P}} \approx \pi\sqrt{\frac{(1-\upsilon_1)E_1}{(1+\upsilon_1)(1-2\upsilon_1)\rho_1 h_1^{\,2}}} \tag{40}$$

The LBs of the 1st BG for is obtained by substituting Eq. (39), Eq. (40) and $p=1$ into Eq. (36):

$$\omega_{1-\mathrm{start-S}} \approx \sqrt{\frac{2E_1}{(1+\upsilon_1)\rho_2 h_1 h_2}} \tag{41}$$

$$\omega_{1-\mathrm{start-P}} \approx \sqrt{\frac{4(1-\upsilon_1)E_1}{(1+\upsilon_1)(1-2\upsilon_1)h_1 h_2 \rho_2}} \tag{42}$$

Is evident that BI and $\omega_{1-\mathrm{end}}$ shares the following properties: 1, $\omega_{1-\mathrm{end}}$ or BI is solely only determined by the density, Young's modulus, Poisson's ratio and thickness of the rubber layer; 2, $\omega_{1-\mathrm{end}}$ or BI can be treated as the following power-law functions: $\mathrm{Const}\cdot E_1^{1/2}$, $\mathrm{Const}\cdot \rho_1^{-1/2}$ and $\mathrm{Const}\cdot h_1^{-1}$. On the other hand, $\omega_{1-\mathrm{start}}$ can be written as the following power-law functions: $\mathrm{Const}\cdot E_1^{1/2}$, $\mathrm{Const}\cdot \rho_2^{-1/2}$ and $\mathrm{Const}\cdot h_1 h_2^{-1/2}$. Figs. 10 (a) and (b) show $\omega_{1-\mathrm{end}}$ as a function of both ρ_1 and h_1 for S-wave and P-wave respectively, and Figs. 10 (c) and (d) show $\omega_{1-\mathrm{start}}$ as a function of both ρ_2 and $\sqrt{h_1 h_2}$ for S-wave and P-wave respectively, where the rest material parameters are described in Table 1.

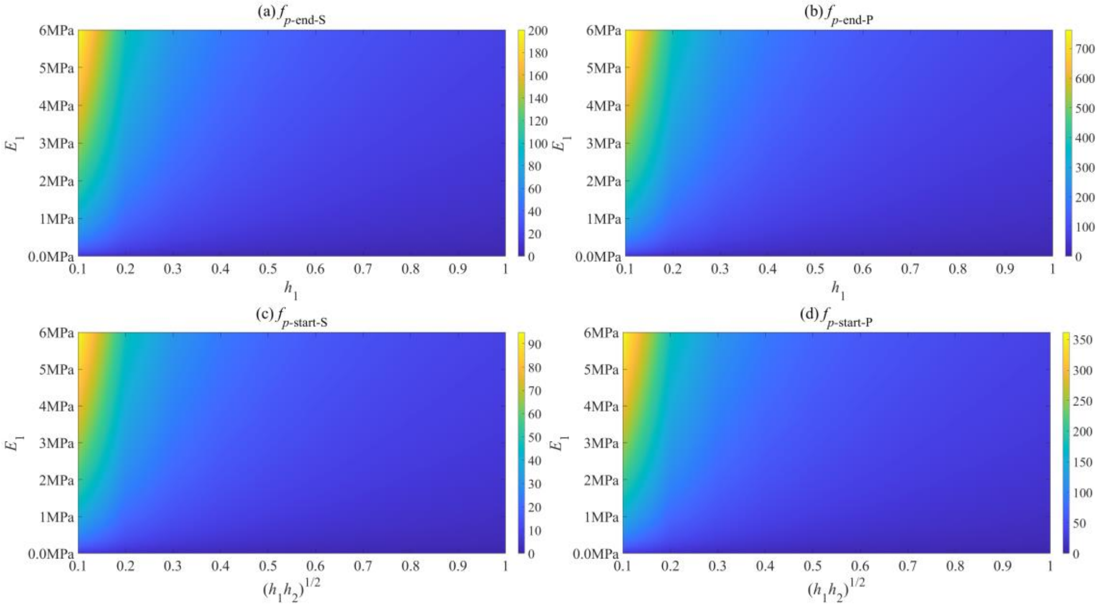

FIGURE 10 Lower bound and upper bound of the first band gap: (a) upper bound for S-wave, (b) upper bound for P-wave, (c) lower bound for S-wave, (d) lower bound for P-wave.

4.4 Approximations of frequency responses

As shown in Fig. 3(a), the curve of LF resembles an ellipse. Accordingly, by using the value of γ at the mid-span and the BG's width as the ellipse's two axes, γ of pth BG can be approximated by

$$\gamma \approx -\ln\left(\left|\Lambda_{1-p-\mathrm{mid}}\right|\right)\sqrt{1-\left[\frac{\omega_l-\omega_{p-\mathrm{mid}}}{(\omega_{p-\mathrm{end}}-\omega_{p-\mathrm{start}})}\right]^2} \tag{43}$$

where $\omega_{p\text{-start}} \le \omega_l \le \omega_{p\text{-end}}$, $\omega_{p-\mathrm{mid}} = \dfrac{\omega_{p-\mathrm{end}}+\omega_{p-\mathrm{start}}}{2}$, $\left|\Lambda_{1-p-\mathrm{mid}}\right| = \dfrac{\left|\mathrm{trace}_{p-\mathrm{mid}}\right|-\sqrt{\mathrm{trace}_{p-\mathrm{mid}}^{\;2}-4}}{2}$, and $\mathrm{trace}_{p-\mathrm{mid}} = 2\cos\left(\dfrac{h_1}{c_1}\omega_{p-\mathrm{mid}}\right)\cos\left(\dfrac{h_2}{c_2}\omega_{p-\mathrm{mid}}\right)-2D\sin\left(\dfrac{h_1}{c_1}\omega_{p-\mathrm{mid}}\right)\sin\left(\dfrac{h_2}{c_2}\omega_{p-\mathrm{mid}}\right)$. And AC becomes

$$r \approx 1-\exp\left\{\ln\left(\Lambda_{1-p-\mathrm{mid}}\right)\sqrt{1-\left[\frac{\omega_l-\omega_{p-\mathrm{mid}}}{(\omega_{p-\mathrm{end}}-\omega_{p-\mathrm{start}})}\right]^2}\right\} \tag{44}$$

The approximation for the FR matrix is obtained by substituting Eq. (25) into Eq. (44), i.e.:

$$\mathbf{FR} \approx \exp\left\{ n \ln\left(\Lambda_{1-p-\mathrm{mid}}\right) \sqrt{1-\left[\frac{\omega_l-\omega_{p-\mathrm{mid}}}{\left(\omega_{p-\mathrm{end}}-\omega_{p-\mathrm{start}}\right)}\right]^2} \right\} \begin{bmatrix} \left|\cos\theta\right| & \left|\sin\theta\tan\phi\right| \\ \left|\sin\theta\tan\phi\right| & \left|\cos\theta\right| \end{bmatrix} \tag{45}$$

Figs. 11 (a)-(d) show the comparison between the exact values and the corresponding approximations for the LF, AC, and FRs under S-waves and P-waves of the benchmark periodic structures. The good match between the exact values and the approximations demonstrates the validity of Eq. (43) to (45).

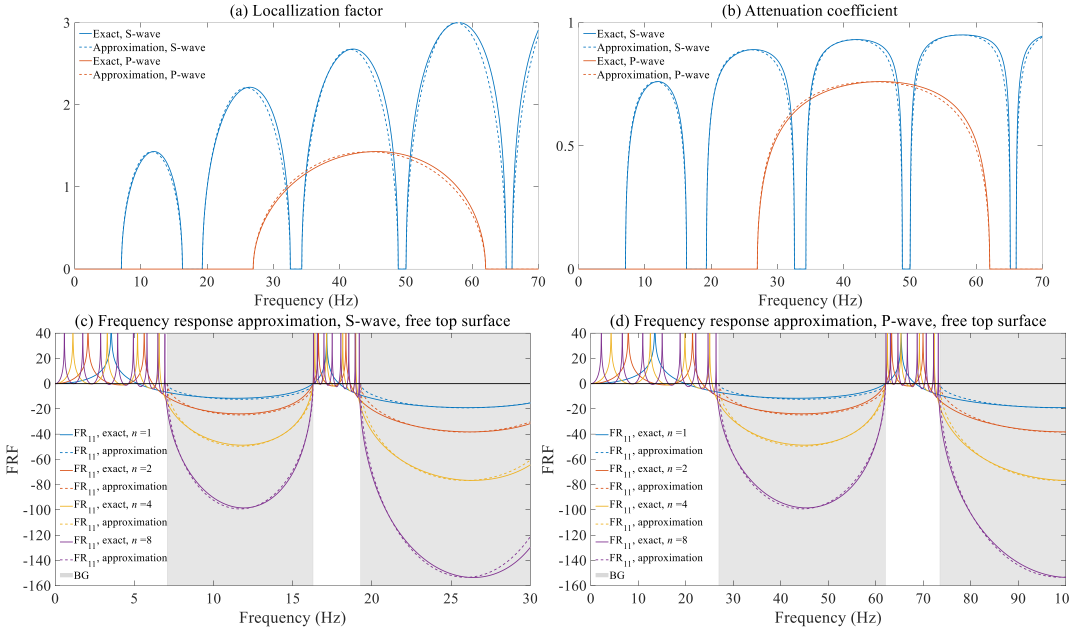

FIGURE 11 Approximations based on elliptical localization factor: (a) localization factor, (b) attenuation coefficient, (c) frequency response for S-wave, (d) frequency response for P-wave.

5.OPTIMAL DESIGN APPROACH FOR ONE-DIMENSIONAL RUBBER-CONCRETE PERIODIC FOUNDATIONS

In Section 4, it is demonstrated that the attenuation effect of BGs is always preserved regardless of the existence of superstructures, which implies we can compute or design the BGs without further considering superstructure-foundation couple effects. This fact enlightens the following convenient optimal design approach of 1-D RC periodic foundations, which takes into consideration both S-waves and P-waves. The core idea of this design approach is to optimally fill the superstructures' resonance frequencies into first few BGs, and at time same time maximize the performance function.

5.1 Problem statement

Given a 1-D RC periodic foundation to design and a superstructure with a series resonance zones (RZs), in which: the frequency band of seismic ground motions to attenuate is $\mathrm{FB}=\left(\omega_{\mathrm{FB-start}},\ \omega_{\mathrm{FB-end}}\right)$, and the parentheses represent an open inerval; the set of RZs for S-waves is denoted by $\mathbf{RZ}_{\mathrm{S}}$, and the q^{th} element is $\mathrm{RZ}_{q-\mathrm{S}}=\left(\omega_{q-\mathrm{start-RZ_S}},\ \omega_{q-\mathrm{end-RZ_S}}\right)$; the set of RZs for P-waves is denoted by $\mathbf{RZ}_{\mathrm{P}}$, and the r^{th} element is $\mathrm{RZ}_{r-\mathrm{P}}=\left(\omega_{r-\mathrm{start-RZ_P}},\ \omega_{r-\mathrm{end-RZ_P}}\right)$; the p^{th} BGs for S-waves and P-waves are denoted by $\mathrm{BG}_{p-\mathrm{S}}=\left(\omega_{p-\mathrm{start-S}},\ \omega_{p-\mathrm{end-S}}\right)$ and $\mathrm{BG}_{p-\mathrm{P}}=\left(\omega_{p-\mathrm{start-P}},\ \omega_{p-\mathrm{end-P}}\right)$ respectively; the performance function $\mathrm{PF}(h_1, h_2)$ measures the goodness of the foundation's design (e.g., $\mathrm{PF}(h_1, h_2)=n$ since maximizing the number of unit-cells would efficiently increase the attenuation effect). A good design of the 1-D RC periodic foundation should ensure the FRs of the superstructure is fairly alleviated for any frequency within the consideration, which requires every RZ being covered by a corresponding BG. Besides, for all potential designs that meet above requirement, the optimal one should also maximize $\mathrm{PF}(h_1, h_2)$. Hence, as shown in Fig. 12, the optimization problem becomes the search for h_1 and h_2 maximizing $\mathrm{PF}(h_1, h_2)$ on condition that: 1, any $\mathrm{RZ}_{q-\mathrm{S}}$ in FB should belong to a $\mathrm{BG}_{p-\mathrm{S}}$; 2, any $\mathrm{RZ}_{q-\mathrm{P}}$ in FB should belong to a $\mathrm{BG}_{p-\mathrm{P}}$; 3, the configuration constrain $\mathrm{CC}(h_1,\ h_2, n)$ is satisfied, e.g., $\mathrm{CC}(h_1,\ h_2, n)=n(h_1+h_2)<H_{\max}$, $H_{\max}$ is the allowed foundation height.

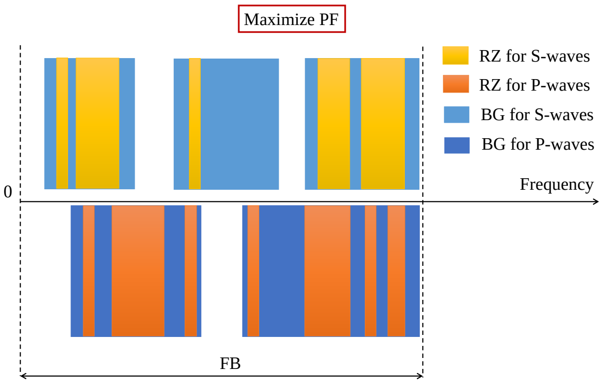

FIGURE 12 Problem statement of the optimal design.

5.2 Approach presentation

According to the optimization problem stated in subsection 5.1, a design approach is presented in this subsection based on the assumption that $\mathrm{PF}(h_1, h_2)$ is a monotonic decreasing function of $h_1 + h_2$, since this assumption is in accordance of many different choices of PF, e.g., PF=n, or PF represents the least amount of the cost of materials. As shown in Fig. 13, the design approach consists of the following steps:

1. Determine the FB based on anti-seismic requirements;
2. Determine the RZs to attenuate according to the superstructure's FRs and FB, e.g., the superstructure has three RZs namely (2.5, 4.5) Hz, (10.1, 20.1) Hz and (40.4, 60.6) Hz. if FB= (5.0 50.0) Hz, then RZ=(2.5, 4.5) Hz is rejected since it is outside the FB, RZ=(10.1, 20.1) Hz is accepted since it is contained by the FB, and RZ=(40.4, 60.6) Hz is altered to (40.4, 50.0) then accepted;
3. Map every $\mathrm{RZ}_{r-\mathrm{P}}$ into the corresponding RZ for S-waves, denoted by $\mathrm{RZ}_{r-\mathrm{S}}$, according to Eq. (38), and add it to $\mathbf{RZ}_{\mathrm{S}}$, i.e., $\mathrm{RZ}_{r\text{-}\mathrm{S}} = \left(\mathrm{MR}\omega_{r-\mathrm{start}-\mathrm{RZ}_{\mathrm{P}}},\ \mathrm{MR}\omega_{r-\mathrm{end}-\mathrm{RZ}_{\mathrm{P}}}\right)$;
4. Merge overlapped elements in $\mathbf{RZ}_{\mathrm{S}}$, e.g., $\mathrm{RZ}_{q-\mathrm{S}} = (3.3, 5.5)$, $\mathrm{RZ}_{r-\mathrm{S}} = (4.4, 6.6)$, then delete both $\mathrm{RZ}_{q-\mathrm{S}}$ and $\mathrm{RZ}_{r-\mathrm{S}}$ from $\mathbf{RZ}_{\mathrm{S}}$, then insert $\mathrm{RZ}_{t-\mathrm{S}} = (3.3, 6.6)$ into it;
5. Enumerate every element $\mathrm{RZ}_{t-\mathrm{S}}$ in $\mathbf{RZ}_{\mathrm{S}}$ with Step 6;
6. Exhaust every p in $1 \le p \le p_{\max}$ with Step 7 to 9 and Step 15;
7. Assume the UB of $\mathrm{RZ}_{t-\mathrm{S}}$ is equal to the UB of $\mathrm{BG}_{p-\mathrm{S}}$ and compute the trail $\mathrm{BI}_{\mathrm{S-trail}}$, i.e.,
$$\mathrm{BI}_{\mathrm{S-trail}} = \frac{\omega_{t-\mathrm{end}-\mathrm{RZ}_{\mathrm{S}}}}{p};$$
8. Check the validity of $\mathrm{BI}_{\mathrm{S-trail}}$ by testing if none of the BGs' UBs cuts an element in $\mathbf{RZ}_{\mathrm{S}}$, i.e., $\mathrm{BI}_{\mathrm{S-trail}}$ is valid if $\left[\frac{\omega_{s-\mathrm{start}-\mathrm{RZ}_{\mathrm{S}}}}{\mathrm{BI}_{\mathrm{S-trail}}}\right] = \left[\frac{\omega_{s-\mathrm{end}-\mathrm{RZ}_{\mathrm{S}}}}{\mathrm{BI}_{\mathrm{S-trail}}}\right]$ for any $\mathrm{RZ}_{s-\mathrm{S}}$ in $\mathbf{RZ}_{\mathrm{S}}$, where the brackets represent the operator of getting integer part;
9. For a valid $\mathrm{BI}_{\mathrm{S-trail}}$, perform Step 10 to 11 to obtain the corresponding the trail thickness of rubber layer and concrete layer denoted by $h_{1-\mathrm{trail}}$ and $h_{2-\mathrm{trail}}$, respectively;
10. Compute $h_{1-\mathrm{trail}}$ according to Eq. (39), i.e., $h_{1-\mathrm{trail}} = \dfrac{\pi}{\mathrm{BI}_{\mathrm{S-trail}}}\sqrt{\dfrac{E_1}{2(1+\upsilon_1)\rho_1}}$;
11. Obtain $h_{2-\mathrm{trail}}$ by performing Step 12 to 14 for every $\mathrm{RZ}_{u-\mathrm{S}}$ in $\mathbf{RZ}_{\mathrm{S}}$;
12. Assume the LB of $\mathrm{RZ}_{u-\mathrm{S}}$ equals the BG's LB and compute $h_{2-\mathrm{temp}}$ according to Eq. (33), i.e.,
$$h_{2-\mathrm{temp}} = \frac{2c_2 h_{1-\mathrm{trail}}}{Dc_1\left\{\left(\omega_{u-\mathrm{start}-\mathrm{RZ}_{\mathrm{S}}}\dfrac{h_{1-\mathrm{trail}}}{c_1} - \dfrac{\pi}{2}\right)^2 - \left(\dfrac{\pi}{2}\left[\dfrac{\omega_{s-\mathrm{start}-\mathrm{RZ}_{\mathrm{S}}}}{\mathrm{BI}_{\mathrm{S-trail}}}\right]\right)^2\right\}};$$
13. Insert $h_{2-\mathrm{temp}}$ into the set $\mathbf{h}_{2-\mathrm{temp}}$;
14. Obtain $h_{2-\mathrm{trail}}$ by choosing the maximum element of $\mathbf{h}_{2-\mathrm{temp}}$ i.e., $h_{2-\mathrm{trail}} = \max(h_{2-\mathrm{temp}})$;

15. Compute the trail performance function $\mathrm{PF}_{\mathrm{trail}} = \mathrm{PF}\left(h_{1-\mathrm{trail}},\ h_{2-\mathrm{trail}}\right)$ and insert to $\mathbf{PF}_{\mathrm{trail}}$;
16. Search for the maximum of $\mathbf{PF}_{\mathrm{trail}}$, i.e., $\mathrm{PF}_{\max} = \mathrm{PF}\left(h_{1-\mathrm{opt}},\ h_{2-\mathrm{opt}}\right) = \max(\mathrm{PF}_{\mathrm{trail}})$, and $h_{1-\mathrm{opt}}$, $h_{2-\mathrm{opt}}$ are the optimal thickness of the rubber layer and concrete layer respectively;
17. Compute the max number of unit cells on condition that the configuration constrain $\mathrm{CC}(h_{1-\mathrm{opt}},\ h_{2-\mathrm{opt}}, n)$ is satisfied.

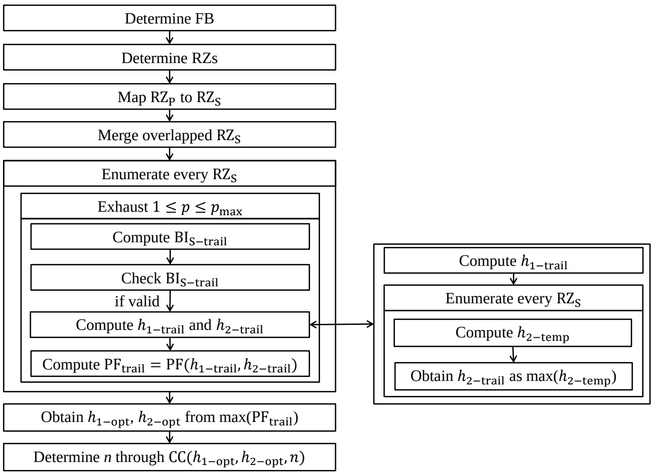

FIGURE 13 Flowchart of the optimal design approach.

5.3 Theoretical explanation

Firstly, since BGs and RZs for P-waves can be one-to-one mapped to the corresponding quantities for S-waves, it is sufficient to consider cases of S-waves only. Suppose there is a set of $\mathrm{RZ}_{t-\mathrm{S}} = \left(\omega_{t-\mathrm{start-RZ_S}},\ \omega_{t-\mathrm{end-RZ_S}}\right)$ denoted by $\mathbf{RZ}_{\mathrm{S}} = \left\{\mathrm{RZ}_{t-\mathrm{S}},\ 1 \le t \le t_{\max}\right\}$ and a set of $\mathrm{BG}_{p-\mathrm{S}} = (\omega_{p-\mathrm{start-S}},\ \omega_{p-\mathrm{end-S}})$ denoted by $\mathbf{BG}_{\mathrm{S}} = \left\{\mathrm{BG}_{p-\mathrm{S}},\ 1 \le p \le p_{\max}\right\}$, each $\mathrm{RZ}_{t-\mathrm{S}}$ is embedded in a $\mathrm{BG}_{p-\mathrm{S}}$. According to Eq. (37), $\mathbf{RZ}$ can be mapped to the 1st BG to form a new set that denoted by $\mathbf{RZ}_{\mathrm{MP1}} = \left\{\mathrm{RZ}_{i-\mathrm{MP1}},\ 1 \le i \le m\right\}$. The LB and UB of $\mathbf{RZ}_{\mathrm{MP1}}$ are $\omega_{\mathrm{start-MP1}}$ and $\omega_{\mathrm{end-MP1}}$ respectively. As shown in Fig. 14, the distances between 0 to $\omega_{\mathrm{start-MP1}}$, $\omega_{\mathrm{1\text{-}start\text{-}S}}$ to $\omega_{\mathrm{start-MP1}}$, 0 to $\omega_{\mathrm{end-MP1}}$, and $\omega_{\mathrm{end-MP1}}$ to $\omega_{\mathrm{1\text{-}end\text{-}S}}$ are respectively Δ_1, Δ_2, Δ_3 and Δ_4, where $\Delta_2 \ge 0$ and $\Delta_4 \ge 0$. By using Eq. (39) and Eq. (41), it is computed that $h_1 = \dfrac{\pi}{\Delta_3 + \Delta_4}\sqrt{\dfrac{E_1}{2(1+\upsilon_1)\rho_1}}$, and $h_2 = \dfrac{2(\Delta_3+\Delta_4)}{\pi\rho_2(\Delta_1-\Delta_2)^2}\sqrt{\dfrac{2\rho_1 E_1}{(1+\upsilon_1)}}$. Since it is assumed that $\mathrm{PF}(h_1, h_2)$ is a monotonic decreasing function of $h_1 + h_2$, the optimal design is charactered by $\min[h_1 + h_2]$. Because $\dfrac{\mathrm{d}(h_1+h_2)}{\mathrm{d}\Delta_2} = \dfrac{\mathrm{d}h_2}{\mathrm{d}\Delta_2} = \dfrac{4(\Delta_3+\Delta_4)}{\pi\rho_2(\Delta_1-\Delta_2)^3}\sqrt{\dfrac{2\rho_1 E_1}{(1+\upsilon_1)}} > 0$, $\min[h_1+h_2]$ is reached when $\Delta_2 = 0$, which yields $h_1 + h_2 = \dfrac{\pi}{\Delta_3+\Delta_4}\sqrt{\dfrac{E_1}{2(1+\upsilon_1)\rho_1}} + \dfrac{2(\Delta_3+\Delta_4)}{\pi\rho_2\Delta_1^2}\sqrt{\dfrac{2\rho_1 E_1}{(1+\upsilon_1)}}$. Similarly, $\dfrac{\mathrm{d}(h_1+h_2)}{\mathrm{d}\Delta_4} = \left[\dfrac{4}{\pi\rho_2\Delta_1^2} - \dfrac{\pi}{(\Delta_3+\Delta_4)^2\rho_1}\right]\sqrt{\dfrac{E_1\rho_1}{(1+\upsilon_1)}} > 0$ if $\dfrac{\rho_1}{\rho_2} > \left(\dfrac{\pi\Delta_1}{2\Delta_3}\right)^2$. Therefore, $h_1 + h_2$ reaches the minimum when $\Delta_1 = \Delta_2 = 0$, which means the optimal design must ensure that the LB of q^{th} BG is equal to the LB of s^{th} RZ, and the UB of p^{th} BG is equal to the UB of t^{th} RZ. Thus, the optimal design can be obtained by exhausting all possible combinations of *p*, *q*, *r* and *s*. The proposed design approach is literally a traversal algorithm for all the combinations, which guarantees the final output for the design is optimal in a global sense. To be specific, Step 5 to Step 7 collect all possible values of BI by assuming $\omega_{p-\mathrm{end-S}} = \omega_{t-\mathrm{end-RZ_S}}$. In addition, BI should separate RZs into groups without cutting an RZ, so Step 8 rejects the invalid values of BI by examining if there exist an $\omega_{p-\mathrm{end-S}}$ locating in a RZ. After a valid BI is determined, the next task is to find the corresponding combination of h_1 and h_2, while h_1 is directly computed in Step 10 through Eq. (39). Then by assuming $\omega_{p-\mathrm{start-S}} = \omega_{r-\mathrm{start-RZ_S}}$, a trail h_2

can be computed by using Eq. (33). From Eq. (36) it is known that o_p is a monotonic increasing function of h_2. This means the largest trail h_2 after enumerating every possible combination for $\omega_{p-\text{start}-\text{S}} = \omega_{r-\text{start}-\text{RZ}_\text{S}}$ is the valid value of h_2 the current BI, which is spirit of Step 11 to 14. The optimal combination of h_1 and h_2 is the one that maximizing the performance function. Therefore, by choosing the maximum value of performance function for all combinations of h_1 and h_2, $h_{1-\text{opt}}$ and $h_{2-\text{opt}}$ can be obtained, which is performed in Step 15 to 16. Finally, the number of unit cells can be consequently computed by Step 17.

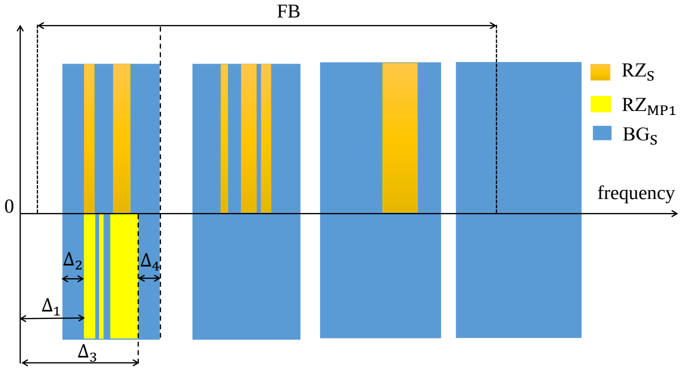

FIGURE 14 Diagrammatic sketch for the illustration on optimality.

5.4 Design example

As to further demonstrate its the practicality and the performance, the proposed approach is applied to design an optimal 1-D RC periodic foundation for the steel frame described by Table 2 undertaking a board range of ground motion vibrations. The periodic foundation to design is a 10 m by 10 m square foundation with a maximum depth equals 4 m, in which the materials to use are rubber and concrete described by Table 1. In the design process, FB was determined to be 2.5 to 60.0 Hz. Firstly, the FRFs of the steel frame are computed through ABAQUS 6.14 using the "SteadyStateDirectStep", in which the FRFs for S-wave and P-wave re obtained by assigning the 4 bottom nodes a unit displacement in X-direction and in Y-direction respectively. Then $\mathbf{RZ}_\text{S}$ and $\mathbf{RZ}_\text{P}$ were determined by checking if the FRFs in FB are greater than the corresponding thresholds, in which the thresholds for S-saves and P-waves are respectively 0.0 and 3.0. The consideration for the threshold of $\mathbf{RZ}_\text{P}$ being larger than that of $\mathbf{RZ}_\text{S}$ is because horizontal ground motions are usually more dangerous. As shown in Figs. 15, $\mathbf{RZ}_\text{S}$ was determined to be the following set of 10 frequency intervals in Hz: 3.1048~3.4789, 6.6254~7.0567, 12.1200~14.4425, 23.5164~23.8595, 29.2337~29.5127, 30.8233~31.8888, 34.8555~35.5267, 36.8418~37.3217, 42.4463~43.0980; and $\mathbf{RZ}_\text{P}$ was: 15.6794~15.9477, 19.6386~21.9264, 22.4521~32.5955, 38.8794~60.0. Afterward, the program realizing the optimal design approach presented in subsection 5.2 was developed in MATLAB and implemented to the optimal design, from which the optimal thicknesses of rubber layer and concrete layer are calculated to be 0.3779 m and 0.6555 respectively. The results of designed AZs and BGs using the predicted optimal configuration are shown in Fig. 16, from which it is seen that all the AZs are well distributed in BGs with minimum waste. Finally, after practical consideration of manufacturing, the thickness for rubber layer and concrete layer are determined to be 0.36 m and 0.64 m, and the number of unit cells is 4.

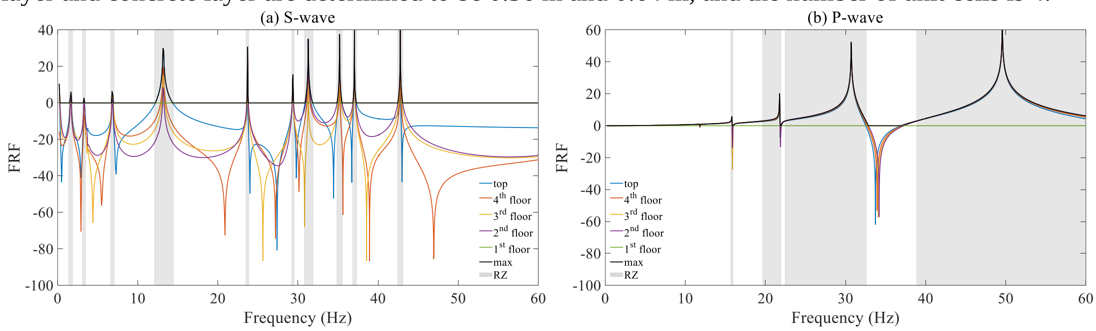

FIGURE15 Frequency responses and resonance zones of the superstructure: (a) S-wave, (b) P-wave.

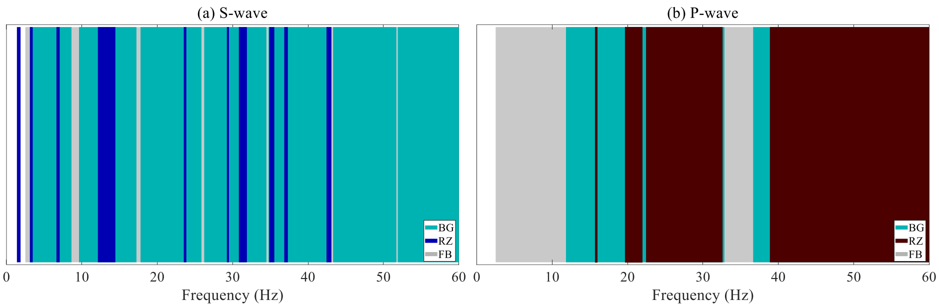

FIGURE 16 Band gaps and resonance zones of the optimal design: (a) S-wave, (b) P-wave.

5.5 Numerical validation

To further verify the optimality of the proposed design approach, the performances of the optimally designed foundation, the concrete foundation and the benchmark foundation were compared numerically. The FEM analyses for the optimally designed foundation and the concrete foundation were similar to the analysis of the benchmark foundation introduced in subsection 3.3, in which the thicknesses of rubber layer and concrete layer were changed to 0.36 m and 0.64 m respectively for the optimally designed foundation, and the material for layer 1 is concrete for the concrete foundation. Figs. 17 show the simulation results of the FRFs of each floor of the steel frame with respective these three different foundations. It is seen that the optimally designed foundation dramatically outperforms the concrete foundation and the benchmark foundation for both the case of S-waves and the case of P-waves. Moreover, the vibration attenuation performance of the optimally designed foundation for S-waves is extremely outstanding that nearly all FRFs in FB are smaller than 0 and the majority is even lower than -50, while benchmark foundation failed to attenuate the AZs outside the BGs. Besides, the attenuation effect of the optimally designed foundation is expected to be even better if the configuration can strictly follow the result yield from the proposed approach. However, the attenuation performance for P-waves is relatively ordinary due to the higher threshold of FRF for $\mathbf{RZ}_{P}$, which is acceptable since the case of P-waves rather than P-waves is not the primary design objective.

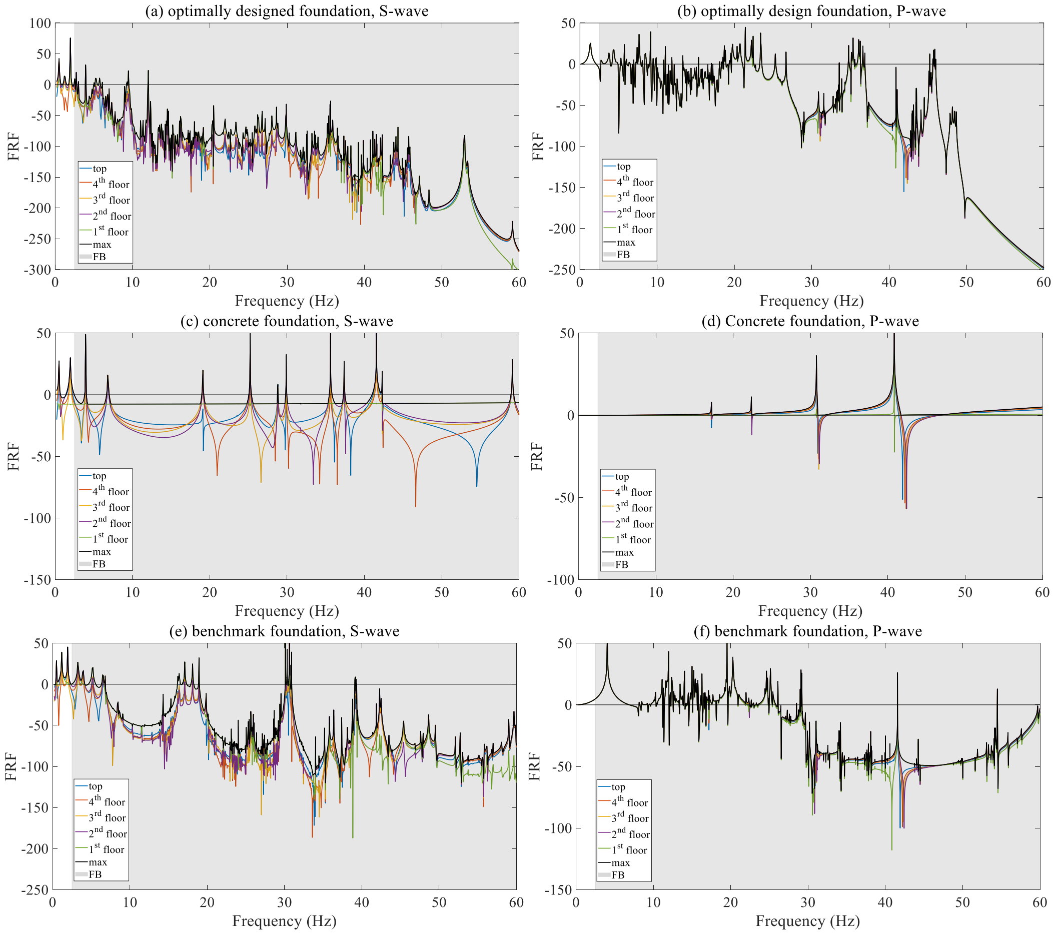

FIGURE 17 Frequency responses of the exemplary superstructure with different foundations.

6. CONCLUSION

This research studies frequency related properties of 1-D periodic structures, emphasizing on the seismic vibration related issues of 1-D RC periodic foundations. Based on the characteristics of BGs, an optimal approach for designing 1-D RC periodic foundations is proposed and validified both theoretically and numerically. Moreover, the following critical conclusions are drawn:

1. FRs of 1-D periodic structures can be computed by substituting the boundary conditions to the FR matrix;
2. On conditional that the number of unit cells is sufficient, the FR matrix can be approximately calculated by using the AC and the eigen direction of the transfer matrix;
3. The attenuation effect of BGs is consistently preserved regardless of the existence of superstructure;
4. The first few BGs of 1-D RC periodic foundations can be accurately approximated by the proposed analytical formulas;
5. AC and FRs of 1-D RC periodic foundations can be well-approximated by employing an elliptical shaped LF.
6. The proposed design approach for 1-D RC periodic foundations is globally optimal.

7.ACCKNOWLEDGEMENT

The authors wish to acknowledge the support provided by the National Natural Science Foundation of China (No. 52078395), the Open Projects Foundation of Sate Key Laboratory for Health and Safety of Bridge Structure (No. BHSKL19-07-GF) and Science Research Foundation of Wuhan Institute of Technology (No. K2021030).

8.REFERENCE

1. Shah A, Datta S. Harmonic waves in a periodically laminated medium. *International Journal of Solids and Structures*. 1982;18(5):397-410.
2. Delph T, Herrmann G, Kaul R. Harmonic wave propagation in a periodically layered, infinite elastic body: plane strain, analytical results. *Journal of Applied Mechanics*. 1979;
3. Mead D. Wave propagation in continuous periodic structures: research contributions from Southampton, 1964–1995. *Journal of sound and vibration*. 1996;190(3):495-524.
4. Xiong C, Shi Z, Xiang H. Attenuation of building vibration using periodic foundations. *Advances in Structural Engineering*. 2012;15(8):1375-1388.
5. Yu D, Wen J, Zhao H, Liu Y, Wen X. Vibration reduction by using the idea of phononic crystals in a pipe-conveying fluid. *Journal of Sound and vibration*. 2008;318(1-2):193-205.
6. Chen A-L, Wang Y-SJPBCM. Study on band gaps of elastic waves propagating in one-dimensional disordered phononic crystals. *Physica B*. 2007;392(1-2):369-378.
7. Xiang H-J, Shi Z-F. Analysis of flexural vibration band gaps in periodic beams using differential quadrature method. *Computers & structures*. 2009;87(23-24):1559-1566.
8. Cheng Z, Shi Z. Novel composite periodic structures with attenuation zones. *Engineering Structures*. 2013;56:1271-1282.
9. Yan Y, Laskar A, Cheng Z, et al. Seismic isolation of two dimensional periodic foundations. *Journal of Applied Physics*. 2014;116(4):044908.
10. Yan Y, Cheng Z, Menq F, Mo Y, Tang Y, Shi Z. Three dimensional periodic foundations for base seismic isolation. *Smart Materials and Structures*. 2015;24(7):075006.
11. Wang Y-F, Liang J-W, Chen A-L, Wang Y-S, Laude V. Wave propagation in one-dimensional fluid-saturated porous metamaterials. *Physical Review B*. 2019;99(13):134304.
12. Witarto W, Wang S, Yang C, et al. Three-dimensional periodic materials as seismic base isolator for nuclear infrastructure. *AIP Advances*. 2019;9(4):045014.
13. Sigalas M, Economou EN. Band structure of elastic waves in two dimensional systems. *Solid state communications*. 1993;86(3):141-143.
14. Kafesaki M, Sigalas M, Economou E. Elastic wave band gaps in 3-D periodic polymer matrix composites. *Solid state communications*. 1995;96(5):285-289.
15. Shimotsuma Y, Kazansky PG, Qiu J, Hirao K. Self-organized nanogratings in glass irradiated by ultrashort light pulses. *Physical review letters*. 2003;91(24):247405.
16. Wang L-G, Zhu S-Y. Electronic band gaps and transport properties in graphene superlattices with one-dimensional periodic potentials of square barriers. *Physical Review B*. 2010;81(20):205444.
17. Sánchez-Pérez JV, Caballero D, Mártinez-Sala R, et al. Sound attenuation by a two-dimensional array of rigid cylinders. *Physical Review Letters*. 1998;80(24):5325.
18. Basone F, Wenzel M, Bursi OS, Fossetti M. Finite locally resonant metafoundations for the seismic protection of fuel storage tanks. *Earthquake Engineering & Structural Dynamics*.

2019;48(2):232-252.
19. Cheng Z, Shi Z. Composite periodic foundation and its application for seismic isolation. *Earthquake Engineering & Structural Dynamics*. 2018;47(4):925-944.
20. Jia G, Shi Z. A new seismic isolation system and its feasibility study. *Earthquake Engineering and Engineering Vibration*. 2010;9(1):75-82.
21. Cheng Z, Shi Z, Palermo A, Xiang H, Guo W, Marzani A. Seismic vibrations attenuation via damped layered periodic foundations. *Engineering Structures*. 2020;211:110427.
22. Sun F, Xiao L, Bursi OS. Optimal design and novel configuration of a locally resonant periodic foundation (LRPF) for seismic protection of fuel storage tanks. *Engineering Structures*. 2019;189:147-156.
23. Zhao C, Zeng C, Witarto W, wen Huang H, Dai J, Mo Y. Isolation performance of a small modular reactor using 1D periodic foundation. *Engineering Structures*. 2021;244:112825.
24. Witarto W, Wang S, Nie X, et al. Analysis and design of one dimensional periodic foundations for seismic base isolation of structures. *International Journal of Engineering Research and Applications*. 2016;6(1):5-15.
25. Bao J, Shi Z, Xiang HJJoEM. Dynamic responses of a structure with periodic foundations. *Journal of Engineering Mechanics*. 2012;138(7):761-769.
26. Xiang H, Shi Z, Wang S, Mo Y. Periodic materials-based vibration attenuation in layered foundations: experimental validation. *Smart Materials and Structures*. 2012;21(11):112003.
27. Shi Z, Huang J. Feasibility of reducing three-dimensional wave energy by introducing periodic foundations. *Soil Dynamics and Earthquake Engineering*. 2013;50:204-212.
28. Sackman J, Kelly J, Javid A. A layered notch filter for high-frequency dynamic isolation. *Journal of Pressure Vessel Technology* 1989;
29. Shi Z, Cheng Z, Xiang H. Seismic isolation foundations with effective attenuation zones. *Soil Dynamics and Earthquake Engineering*. 2014;57:143-151.
30. Witarto W, Wang S, Yang C, et al. Seismic isolation of small modular reactors using metamaterials. *AIP Advances*. 2018;8(4):045307.